Materials Advances

ROYAL SOCIETY OF CHEMISTRY

PAPER

View Article Online
View Journal | View Issue

Open Access Article. Published on 16 December 2020. Downloaded on 2/10/2026 7:47:04 PM.
This article is licensed under a Creative Commons Attribution-NonCommercial 3.0 Unported Licence.

Check for updates

Cite this: *Mater. Adv.*, 2021, **2**, 804

Modulated synthesis of thiol-functionalized fcu and hcp UiO-66(Zr) for the removal of silver(I) ions from water†

Bastian Moll, Tim Müller, Carsten Schlüsener, Alexa Schmitz, Philipp Brandt, Secil Öztürk and Christoph Janiak *

Received 30th July 2020,
Accepted 15th December 2020

DOI: 10.1039/d0ma00555j

rsc.li/materials-advances

In recent years there has been a developing interest in the capture of Ag(I) ions from wastewater. In this work we present the synthesis and characterization of two modified thiol-containing UiO-66 metal–organic frameworks (MOFs) capable of removing Ag(I) from aqueous solution. Mercaptoacetic acid (HMAc) was used as a modifier and incorporated as mercaptoacetate into the MOFs. The modulation of the UiO-66 synthesis with HMAc represents an easy and low-cost method for the introduction of thiol groups into the UiO-66 framework, while preserving the general UiO-66 properties like porosity and stability. The usage of very high equivalents of HMAc in relation to $ZrCl_4$ led to reproducible formation of the rare hexagonal close packed (**hcp**) topology of UiO-66 instead of its common face-centered cubic (**fcu**) packing. The materials showed a maximum uptake for Ag(I) from aqueous solutions of over 84 mg g^{-1} for the **fcu** structure and 36 mg g^{-1} for the **hcp** structure. The uptake follows a Langmuir type behavior for both topologies. Uptake kinetics indicates a pseudo second-order rate law for the initial uptake before diffusion control takes over.

Introduction

Metal–organic frameworks (MOF) are potentially porous materials built by organic ligands connected to metal nodes.[1,2] Zirconium(IV)-based MOFs are widely studied[3] and show relatively high chemical[4] and hydrothermal stability.[5] They are promising materials for applications in catalysis,[6] gas storage/separation[7] and for drug delivery.[8] Functionalized zirconium MOFs (Zr-MOFs), especially UiO-66,[9,10] a relatively water-stable MOF with the organic linker benzene-1,4-di-carboxylate (BDC^{2-}),[4] showed promising potential for wastewater treatment as it is capable of removing heavy metal ions of mercury[11,12] and chromium[13] or other impurities.[14–17,24] In addition UiO-66 is regarded as non-toxic, which is of great importance for the purification of water.[18–20]

Thiol-modified Zr-MOFs should be useful for the uptake or removal of soft Lewis-acid metal cations like Hg^{2+} and Ag^{+} from water. To this day few thiol modifications of UiO-66 have been reported in the literature and were synthesized from thiol-functionalized linkers[12,13,21] through postsynthetic linker exchange or linker modification.[12] Yee *et al.* described the synthesis with 2,5-dimercapto-1,4-benzenedicarboxylic acid (H_2DMBD), yielding UiO-66 type MOFs, which they tested for the removal of Hg^{2+}. Their MOF had incorporated 15 wt% sulfur. However, they observed very high amounts of disulfide groups *via* thiol oxidation. The BET surface area was 513 m^2 g^{-1}, which is around half the BET surface area of unmodified UiO-66.[21] H_2DMBD, as the obvious thiol-functionalized common linker terephthalate, would guarantee a high sulfur content, but is not commercially available and has to be synthesized in a complex 3-step organic synthesis under protective gas.[21–23]

Yang *et al.* reported two UiO-type MOFs with the organic linkers mercaptosuccinic acid (MSA) and dimercaptosuccinic acid (DMSA) forming zirconium fumarate analogs Zr-MSA and Zr-DMSA with ~12 wt% sulfur for Zr-MSA and surface areas of 513 m^2 g^{-1} and 275 m^2 g^{-1}, respectively.[13] Just recently Ding *et al.* postsynthetically introduced rhodanine into UiO-66 (UiO-66-Rd) and amino-functionalized UiO-66-NH_2 (UiO-66-NH_2-Rd). The functionalized MOFs showed BET surface areas of 518–606 m^2 g^{-1}, sulfur contents of less than 5 wt%, and achieved high uptake of silver from aqueous solution but at the expense of a decrease of crystallinity in PXRD and BET surface area.[24]

Silver ions (Ag^{+}) and colloidal silver (silver nanoparticles Ag-NP) are known for their microbiological toxicity[25,26] The toxicity of silver nanoparticles seems to be associated with their release of silver ions into the surrounding media.[27,28] This antimicrobial effect led to numerous applications of silver ions or nanoparticles in consumer goods,[29–31] and in medical applications.[27,32] The massive amount of silver used for such

Institut für Anorganische Chemie und Strukturchemie, Heinrich-Heine-Universität, D-40204 Düsseldorf, Germany. E-mail: janiak@uni-duesseldorf.de

† Electronic supplementary information (ESI) available: Synthesis details, SEM-EDX, NMR, TGA, IR and Raman, Ar sorption, UiO structure description, stability tests, adsorption and kinetic modelling. See DOI: 10.1039/d0ma00555j

© 2021 The Author(s). Published by the Royal Society of Chemistry

Open Access Article. Published on 16 December 2020. Downloaded on 2/10/2026 7:47:04 PM.
This article is licensed under a Creative Commons Attribution-NonCommercial 3.0 Unported Licence.

applications leads to an increasing release of silver nanoparticles and silver ions into wastewater[29,33] and a drastically increased exposure of living organisms and the environment to silver(I) ions and silver nanoparticles. The effects of silver on the human organism are still a widely researched topic. *In vitro* studies showed the accumulation of silver nanoparticles in human tissue and organs.[34] Several *in vitro* studies concentrate on the toxicity of silver sources on cell lines.[35,36] Therefore strategies for the removal of silver sources become more and more important. Until now several materials have been evaluated for the removal of silver, including mercapto-functionalized polymers,[37,38] coffee grounds[39] or inorganic materials like layered hydroxides[40] and mercapto-functionalized nanosized TiO_2.[41] In 2016 Conde-González *et al.* demonstrated the promising properties of MOFs for silver removal by using the MOF HKUST-1 to adsorb silver nanoparticles from water.[42]

We note that in the literature the terms "filtration" or "adsorption" are often used for the metal-thiolate binding in porous materials. Adsorption refers to physisorption, while metal-thiolate binding is chemisorption. To avoid ambiguity, we will use the terms "uptake" or "removal" here. The thiophilic character of silver and mercury metal cations is well-known in the literature and can be explained by the HSAB concept (HSAB = hard and soft acids and bases) where interactions of soft Lewis bases (like thiol or thiolate) and soft Lewis acids are preferred.[43]

It is well established that the addition of monocarboxylic acid modulators, like benzoic acid or acetic acid,[3] can enhance the formation of defects in UiO-MOFs,[44,45] which in turn can improve porosity,[46] stability[47] and even catalytic activity.[6a] In this work we used mercaptoacetic acid (HMAc, Scheme 1) to modulate the synthesis of UiO-66, opening the potential of an easy and low-cost method for the introduction of thiol groups into the UiO-66 framework, while preserving general UiO-66 properties like porosity and stability. The mercaptoacetic acid modulator should be incorporated as mercaptoacetate (MAc^-) into the framework to enhance the uptake capacities of UiO-66 in the removal of silver ions.

When using high amounts of HMAc (100 eq.) *versus* $ZrCl_4$ we identified a change in the structure from the usual UiO-66 face-centered cubic (**fcu**)[48] structure to a hexagonal close packed (**hcp**) structure, which was rarely described in the literature after the first observation in 2018.[49] To the best of our knowledge we herein present the first functionalized structure of a **hcp** UiO-66 MOF. We tested two of the synthesized MOFs for the removal capacities of silver(I) from aqueous solution.

Experimental

Materials and methods

Zirconium(IV) chloride ($ZrCl_4$, purity ≥98%) and potassium cyanide (KCN, purity ≥97%) were obtained from Alfa Aesar, benzene-1,4-dicarboxylic acid (H_2BDC, purity 98%) was obtained from Sigma Aldrich and mercaptoacetic acid (HMAc, purity 98%) was obtained from PanReac AppliChem. All solvents were of analysis grade. All chemicals and solvents were used without further purification. AAS standard solution for silver ($AgNO_3$, with Ag(I) concentration = 1000 mg L^{-1}, stabilized by HNO_3) was obtained from Sigma Aldrich. Ultrapure water was produced with a Merck Millipore Synergy© system.

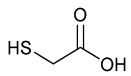

Scheme 1 Structure of mercaptoacetic acid (HMAc).

Powder X-ray diffraction. Powder X-ray diffraction (PXRD) data were acquired with a Bruker D2 Phaser diffractometer using Cu Kα1/α2 radiation with λ = 1.5418 Å at 30 kV. All diffractograms were obtained employing a "low-background sample holder" at 2θ angles from 5–50° at a scan rate 0.125° s^{-1}. Diffractograms for **hcp** UiO-66-MAc-100 eq. were additionally obtained using a Rigaku Miniflex 600 and Cu Kα1/α2 radiation (λ = 1.5418 Å at 40 kV). The samples were measured at 2θ angles from 2–50°.

FT-Infrared (FT-IR). FT-Infrared (FT-IR) spectra were obtained on a Bruker FT-IR Tensor 37 spectrometer with a resolution of 2 cm^{-1} in the 4000–550 cm^{-1} region. All samples were measured as KBr disks.

Raman spectra. Raman spectra were acquired using a Bruker MultiRAM-FT Raman spectrometer equipped with a Nd:YAG-laser. Excitation wavelength of the laser was 1064 nm. All spectra were measured for at least 2500 scans (up to 5000) at a laser intensity of at least 50 mW (up to 700 mW).

Nitrogen (purity 99.9990%) physisorption isotherms. Nitrogen (purity 99.9990%) physisorption isotherms were measured on a Quantachrome Autosorb-6 at 77 K. All samples were activated under a vacuum (1×10^{-3} mbar) and an enhanced temperature of 393 K for 3 h before every sorption measurement. The Brunauer–Emmett–Teller (BET) specific surface area was calculated from the measured nitrogen physisorption isotherms. Multipoint-BET surface areas were determined at relative pressures p/p_0 between 0.01 and 0.05.

Argon (Ar) (purity 99.999%) physisorption experiments. Argon (Ar) (purity 99.999%) physisorption experiments were carried out at 87 K using a Quantachrome Autosorb iQ MP equipped with a Quantachrome cryocooler to adjust the temperature. Total pore volumes were calculated from the Ar-isotherms at p/p_0 = 0.8. Pore size distribution was calculated with QSDFT calculations using the "Ar at 87 K Carbon QSDFT, slit pore, QSDFT equilibrium" model.

Thermogravimetric analysis (TGA). Thermogravimetric analysis (TGA) was performed on a Netzsch Thermo-Microbalance Apparatus TG 209 F3 Tarsus, at a ramp rate of 5 K min^{-1} under a synthetic air flow. All samples were previously dried at 60 °C under a vacuum for at least 12 h.

Scanning electron microscopy (SEM). Scanning electron microscopy (SEM) images were obtained using a Jeol JSM-6510LV QSEM advanced electron microscope equipped with a LaB_6 cathode at 5–20 kV. The microscope was equipped with a Bruker Xflash 410 silicon drift detector for energy-dispersive X-ray (EDX) spectroscopy. The samples were previously dried at 60 °C under a vacuum for at least 12 h. All samples were coated with gold (Au) using a Jeol JFC 1200 finecoater (20 mA for 25 s) before the measurements.

Open Access Article. Published on 16 December 2020. Downloaded on 2/10/2026 7:47:04 PM.
This article is licensed under a Creative Commons Attribution-NonCommercial 3.0 Unported Licence.

UV/Vis spectra. UV/Vis spectra were recorded on an Analytik Jena Specord S 600 (190–1100 nm) in quartz glass cuvettes.

Elemental analysis (CHNS). Elemental analysis (CHNS) was carried out using an Elementar Analysensysteme vario MICRO cube. All samples were previously dried at 60 °C under a vacuum for at least 12 h.

Atomic absorption spectroscopy (AAS). Atomic absorption spectroscopy (AAS) was carried out on a PerkinElmer PinAAcle 900T equipped with a multi-element silver and gold hollow cathode lamp and a 10 cm acetylene-air burner.

1H NMR spectra. ^{1}H NMR spectra were recorded on a Bruker Avance III-600. All samples were dissolved in 1 mol L^{-1} NaOD/D_2O by mixing 20 mg of dried MOF sample with 600 μL of NaOD/D_2O and ultrasonication for 2 h. After the samples were shaken for 4 d (VWR® Mini Shaker at 200 rpm), the samples were again ultrasonicated for 4 h to ensure maximum digestion. Excess MOF and residual ZrO_2 were removed by ultracentrifugation (10 min, 30000 rpm). During the measurements, the d1 relaxation time was set to 20 s and the samples were measured for 128 scans to ensure reliable integrals.

X-ray photoelectron spectroscopy (XPS). X-ray photoelectron spectroscopy (XPS) was conducted on a ULVAC-PHI VersaProbe II microfocus X-ray photoelectron spectrometer. The spectra were recorded with the usage of a polychromatic aluminum Kα X-ray source (1486.8 eV) and referenced to the carbon 1s orbital with a binding energy of 284.8 eV. The CasaXPS, version 2.3.19PR1.0, copyright 1999–2018 Casa Software Ltd program was utilized for the fit of the experimental XP spectra.

Synthesis

All materials were synthesized using a protocol for the synthesis of acetic acid modulated UiO-66,[3] by employing mercaptoacetic acid instead of acetic acid (Scheme 2).

In a typical synthesis, 1 mmol of $ZrCl_4$ (229 mg) and 1 mmol (170 mg) of terephthalic acid (benzene-1,4-dicarboxylic acid, H_2BDC) were mixed with 25 mL of *N*,*N*-dimethylformamide (DMF) and 5 mL of water in a Pyrex bottle with a screw-cap. Mercaptoacetic acid (10–100 eq. in relation to $ZrCl_4$) was added and dissolved under ultrasonification for 10 minutes (for used weights and exact molar ratios see Table S1, ESI†). Afterwards the bottle was placed in an oven and heated to 120 °C for 24 h (ramp time 3 h for heating and 3 h for cooling). The solid product was separated by centrifugation, decanting the supernatant, and washing three times with 35 mL of methanol (MeOH) for 24 h each. Finally, the colorless solid was centrifuged and dried at 60 °C under a vacuum. Obtained yields were between 234 and 249 mg. Products are denoted as UiO-66-MAc-*X*, with *X* = 10, 30, 50 or 100 of used equivalents of HMAc *versus* $ZrCl_4$ in the synthesis. Importantly, the amount of incorporated MAc^- is only between 0.37 and 0.80 eq. However, in the literature it is common to name the samples according to the equivalents of modulator used during the synthesis in relation to the metal salt.[3]

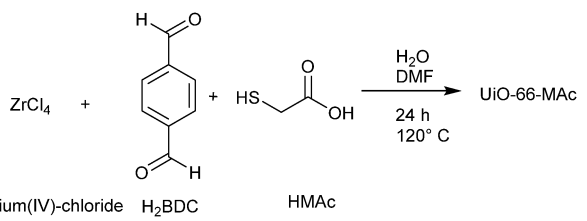

Scheme 2 Reaction scheme for the mercaptoacetic acid (HMAc)-modulated synthesis of UiO-66-Mac.

MOF stability tests. MOF stability tests were conducted by shaking the samples on a VWR® Mini Shaker at 200 rpm for 24 h in ultrapure water (Merck Millipore Synergy©) or in a buffered solution with pH 4 or pH 10. The samples were washed twice with methanol (10 mL each) and dried at 70 °C under air after centrifugation. The products were subsequently examined with PXRD to determine whether decomposition had taken place.

Silver ion removal studies. Silver ion removal studies were conducted as follows: A commercial AAS standard silver(I) nitrate solution (1000 mg L^{-1}, stabilized by HNO_3) was diluted with ultrapure water (Merck Millipore Synergy©) to 2, 10, 50, 100, 250 and 500 mg L^{-1}. Then 10 mg of the dried MOF was mixed with 10 mL of the diluted silver-containing solutions and shaken over night for 12 h under exclusion of light to prevent possible photoreduction of silver. The MOF was separated from the dispersions by centrifugation and decantation and the decanted solution diluted to 1 mg L^{-1} based on their initial concentrations. Silver ion uptake was quantified through AAS determination of the supernatant solution. All silver uptake experiments were carried out twice and the remaining concentration of each batch was determined in triplicate.

Silver ion removal kinetics. Silver ion removal kinetics was followed through AAS. For this purpose, 10 mg of the dried MOF samples were shaken under exclusion of light with 20 mL of a 10 mg L^{-1} silver solution (VWR® Mini Shaker at 200 rpm). After 2, 5, 10, 30, 60 and 120 minutes, samples were taken as described above, diluted to 1 mg L^{-1} based on their initial concentration and measured by AAS. All uptake-kinetic experiments were carried out twice. For further information on the analysis of the silver uptake and the uptake-kinetic studies see Sections S9 and S10, ESI.†

Regeneration studies of the MOFs after Ag(I) uptake. Regeneration studies of the MOFs after Ag(I) uptake were conducted by soaking the Ag-loaded MOFs after the 12 h silver uptake experiments in a freshly prepared aqueous solution of 10 mL of potassium cyanide (500 g L^{-1}) for 24 h on a shaking plate (VWR® Mini Shaker at 200 rpm). All samples were kept under exclusion of light. After decanting the potassium cyanide solution, samples were washed twice with ultrapure water and dried at 60 °C under a vacuum. Samples were investigated by SEM-EDX mapping and PXRD measurements.

Results and discussion

Synthesis and characterization

The synthesis of UiO-66-MAc-*X* from $ZrCl_4$ and terephthalic acid with different equivalents of mercaptoacetic acid as the

 © 2021 The Author(s). Published by the Royal Society of Chemistry

Open Access Article. Published on 16 December 2020. Downloaded on 2/10/2026 7:47:04 PM.
This article is licensed under a Creative Commons Attribution-NonCommercial 3.0 Unported Licence.

modulator yielded colorless solids after drying (Fig. S1, ESI†).[3] The products form small primary particles, which are highly agglomerated (Fig. S2–S5, ESI†), possibly due to the formation of interparticle S–S disulfide bonds on the MOF surface through air oxidation of the thiol groups. The designation of the products as UiO-66-MAc-*X* with *X* = 10, 30, 50 or 100 used equivalents of HMAc in the synthesis followed the general principle of modulated UiOs used in the literature, where the synthesis equivalents of the modulator are indicated, even if the actually incorporated amount is much lower. In our work here, the amount of MAc^- incorporated is only between 0.31 and 0.80 eq. in relation to the organic linker. However, a large excess of modulator can have additional, for example morphological, effects. When Shearer *et al.* investigated the influence of different modulators in the synthesis of UiO-66, the amount of incorporated modulator was only between 0.1 and 0.8 eq. in relation to the organic linker. Yet, an increased amount of modulator (6 to 100 eq.) during the synthesis led to the additional effect of a stepwise phase change from the **fcu** phase of UiO-66 to a primitive cubic **reo** phase.[3] Zhao *et al.* synthesized nano-sized MIL-101(Cr) through the addition of up to 17 eq. of acetic acid (*vs.* Cr and H_2BDC).[50] With increasing equivalents of benzoic acid as modulator (from 3 to 10 eq.) under otherwise similar hydrothermal synthetic conditions. Instead of nanocrystals of MIL-101(Cr) the microparticulated MIL-88B(Cr) product was formed.[51] In 2019 Yang *et al.* had briefly noted the idea of using mercaptoacetic acid as a modulator for the synthesis of a thiol-modified UiO-66 but concentrated on the use of thiol-modified mercaptosuccinate and dimercaptosuccinate linkers for the removal of chromates.[13]

The powder X-ray diffraction (PXRD) patterns of UiO-66-MAc-*X* match the simulated pattern of **fcu** UiO-66 for X = 10, 30, and 50 (Fig. 1).[52] The broadening of the reflexes can be explained through the formation of very small crystallites (Fig. S2–S5, ESI†).

When conducting the synthesis in the presence of 100 eq. HMAc there was a reproducible change in the powder pattern indicating the presence of a different phase (see UiO-66-MAc-100 eq., Fig. 1).

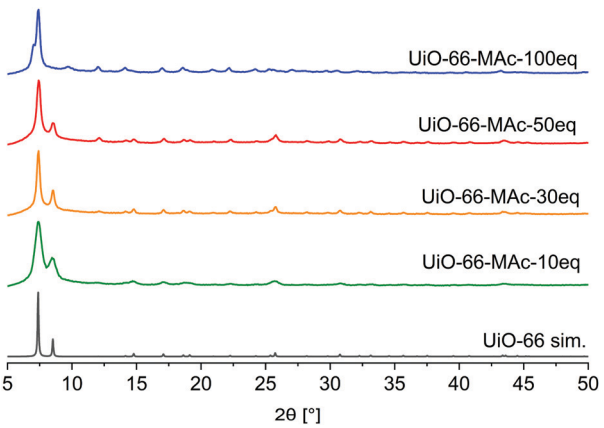

Fig. 1 PXRD patterns of UiO-66-MAc with different HMAc equivalents used in the synthesis and simulated diffractogram of UiO-66 (from CIF CCDC 837796).[52]

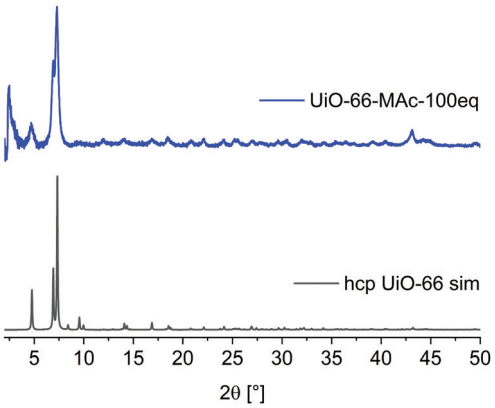

Fig. 2 PXRD pattern of UiO-66-MAc-100 eq. and simulated diffractogram of **hcp** UiO-66 (from CIF CSD-Refcode: KINGUM).[49]

A powder pattern with higher resolution and measured to lower angles of $2\theta < 5°$ (Fig. 2) was in good accordance with the simulated PXRD of the hexagonal close packed (**hcp**) phase of UiO-66, first reported in 2018 by Ermer *et al.*[49]

A brief structural description of **fcu** and **hcp** UiO-66 is provided in Section S7, ESI. †**hcp** UiO-66 was, so far, obtained by either using a terephthalate-containing ionic liquid or poly(ethylene terephthalate) as linker or by using large amounts of hydrochloric acid or acetic acid modulators.[49,53–55] To the best of our knowledge there is no functionalized **hcp** UiO-66 known. PXRD patterns showed the transition to the **hcp** structure starting with the use of ~80 eq. HMAc in relation to $ZrCl_4$ (for details see Section S14, ESI†). The product showed **hcp** reflexes in the PXRD pattern but with poor crystallinity compared to the 100 eq. UiO-66-MAc. This may be due to the formation of both **fcu** and **hcp** phases albeit in small and not well-developed crystallites. The use of 90 eq. HMAc yielded the **hcp** structure of UiO-66. The amount of incorporated MAc^- in UiO-66-MAc was determined by digestion ^{1}H NMR, (details in Section S3, ESI†), and by TGA (details in Section S4, ESI†). All samples were dried before the measurements to ensure a minimal presence of residual solvent. From digestion ^{1}H-NMR and from TGA analysis the molar BDC^{2-} : MAc^- ratios are directly obtained (Table 1). Elemental CHNS analysis (Table S4, ESI†) shows the presence of significant amounts of sulfur but does not provide the possibility to derive a sum formula or linker to modulator ratio because of the undefinable solvent residues. With the sum formulae derived from NMR and TGA, the found wt% sulfur matches the calculated values reasonably well.

In the ideal UiO-66 formula of $[Zr_6O_4(OH)_4(BDC)_6]$ the molar Zr : BDC ratio is 1 : 1. However, UiO-66 is subject to linker defects, which are the basis for MAc incorporation.

The number of linker defects can be calculated from TGA analysis (details Section S4, ESI†) by a procedure from Shearer *et al.*[3] This method is, however, not suitable for the **hcp**-structured UiO-66-MAc-100 eq. because the decomposition does not lead to pure ZrO_2.[49] The comparison of the sulfur contents derived from the linker defect analysis and from CHNS analysis is presented in Section S4 and Table S5, ESI.†

Open Access Article. Published on 16 December 2020. Downloaded on 2/10/2026 7:47:04 PM.
This article is licensed under a Creative Commons Attribution-NonCommercial 3.0 Unported Licence.

Table 1 Determination of incorporated modulator amount in UiO-66-MAc-*X*

UiO-66-MAc-	BDC^{2-} : MAc^{-} ^{1}H-NMR[a]	BDC^{2-} : MAc^{-} TGA[b]	BDC^{2-} : MAc^{-} from defect calc.[c]	BDC^{2-} : MAc^{-} average	Sum formula[d]
10 eq.	1 : 0.30	1 : 0.29	1 : 0.35	1 : 0.31	$Zr_6O_4(OH)_4(BDC)_{4.58}(MAc)_{1.42}$
30 eq.	1 : 0.62	1 : 0.55	1 : 0.50	1 : 0.56	$Zr_6O_4(OH)_4(BDC)_{3.85}(MAc)_{2.15}$
50 eq.	1 : 0.77	1 : 0.85	1 : 0.79	1 : 0.80	$Zr_6O_4(OH)_4(BDC)_{3.33}(MAc)_{2.67}$
100 eq.	1 : 0.64	1 : 0.50	Method not suitable	1 : 0.57	$[(Zr_6O_4(OH)_4)_2(OH)_6](BDC)_{5.73}(MAc)_{3.27}$

[a] Detailed calculation presented in Section S3, ESI. [b] Molar ratios directly determined from weight loss steps. Further details in Section S4, ESI. [c] Sum formula calculated from linker-defect calculations presented in Table S5, ESI. For further details see Section S4, ESI. [d] Sum formula calculated from the average linker to modulator ratios under the assumption that one BDC^{2-} linker in ideal **fcu** UiO-66 with the formula $[Zr_6O_4(OH)_4(BDC)_6]$ and in ideal **hcp** UiO-66 with the formula $[(Zr_6O_4(OH)_4)_2(OH)_6(BDC)_9]$ is replaced by two MAc^{-} molecules.

When the BDC^{2-} linker defects are assumed to be replaced by two MAc^{-} equivalents a BDC^{2-} : MAc^{-} ratio is obtained.

The three BDC^{2-} : MAc^{-} ratios from NMR, TGA and linker-defect analysis agree within experimental error and the average BDC^{2-} : MAc^{-} ratio was taken as the basis for a sum formula (Table 1). In addition, SEM-EDX with elemental mapping allowed us to estimate the Zr:S ratio (Section S2, ESI†). The wt% sulfur from elemental CHNS analysis (Table S5, ESI†) as well as the Zr- and S-EDX mappings show a uniform and concomitant distribution of Zr and S over the entire particles (Section S2, ESI†). The amount of introduced modulator MAc^{-} increased with the amount of used modulator during the synthesis for **fcu** structured UiO-66-MAc-10 eq. to -50 eq. At 100 eq. modulator the UiO-66 phase changed from **fcu** to **hcp**.

At the same time a lower incorporated modulator content was found for the **hcp** structured UiO-66-MAc-100 eq. This correlates with a decreased Zr-BDC-linker ratio of 1 : 0.75 for the **hcp** phase compared to 1 : 1 for the **fcu** structure (see structural information for **fcu** and **hcp** UiO-66 in Section S7, ESI†).

The FT-IR spectra of UiO-66-MAc showed no visible vibrations which can be assigned to the MAc^{-} modulator (Section S5, ESI†). Slight differences in the intensities of the $-CO_2$ linker vibrations between **fcu** structured UiO-66 and the **hcp** phase can be explained by the differences between the SBUs.

However, –SH and C–S vibrations are Raman active and in general show stronger vibration bands compared to the intensities in IR-spectroscopy. In the Raman spectra (Section S5, ESI†) for the 50 eq. and 100 eq. modulated UiOs, signals at 2580 cm^{-1} can be assigned to –SH vibrations (Section S5, ESI†) and were reproducibly visible after enhancing the laser power up to 700 mW and with longer measurements.

The strong agglomeration of primary particles may be due to the formation of interparticle S–S disulfide bonds on the MOF surface after thiol oxidation through oxygen from air. Yee *et al.* reported the formation of disulfide bonds in their 2,5-dimercapto-1,4-benzenedicarboxylate UiO-MOF.[21] There were, however, no characteristic S–S vibrational signals visible in IR- or Raman-spectroscopy in UiO-66-MAc-X (Section S5, ESI†), which indicates that the amount of such S–S bonds, if any, will be very low.

Nitrogen sorption measurements at 77 K of the 10 to 50 eq. **fcu** materials showed a Type IV isotherm with H2 hysteresis (Fig. 3), indicating that the samples are micro- to mesoporous.[56] The mesoporosity can be caused by the linker

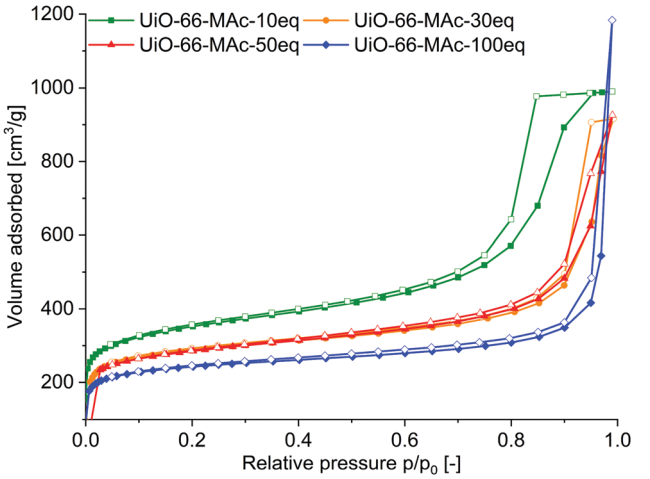

Fig. 3 N_2 sorption isotherms of UiO-66-MAc-10 eq., 30 eq., 50 eq. and 100 eq. at 77 K. Filled symbols: adsorption; empty symbols: desorption.

defects and/or by the aggregation of the nano-sized MOF crystallites, forming meso- (and macroporous) cavities.[57] This aggregation could also be induced by S–S bonds between the crystallites. H2 hysteresis can be attributed to pore-blocking/percolation in a narrow (H2a) or wider (H2b) range of pore necks or to cavitation-induced evaporation. The hysteresis decreased with increasing amounts of modulator. For **hcp** UiO-66-100 eq. the sorption isotherm is a combination of Type I (for the microporosity at low p/p_0) and Type II (at high p/p_0, given by macroporous adsorbents) as the adsorbed multilayer appears to increase without limit when $p/p_0 = 1$. There is only a small hysteresis loop for the **hcp** sample.

The total BET surface area decreased with increasing modulator content (Table 2). BET surface areas of the MAc^{-}-modulated **fcu** MOFs with 1290–1070 $m^2\ g^{-1}$ compare well with the surface areas of unmodulated UiO-66 of 1100 $m^2\ g^{-1}$,[52] and modulated UiO-66 ranging from 700 up to 1600 $m^2\ g^{-1}$.[3,52,58] Also, the BET surface area of **hcp** UiO-66-MAc-100 eq. is in good accordance with the literature values.[49,53–55]

The total surface area was differentiated into the internal micropore surface area (A_{Int}) and the external surface area (A_{Ext}) by the *t*-plot and the *V*–*t*-method (Table 2). The external surface area refers to all non-microporous areas and includes the surface area originating from meso- and macropores, *i.e.* pores with diameters larger than 2 nm. Interestingly, A_{Int} with 825–896 $m^2\ g^{-1}$ did not

© 2021 The Author(s). Published by the Royal Society of Chemistry

Open Access Article. Published on 16 December 2020. Downloaded on 2/10/2026 7:47:04 PM.
This article is licensed under a Creative Commons Attribution-NonCommercial 3.0 Unported Licence.

Table 2 Porosity characteristics of UiO-66-MAc

Material	S_{BET} [a] [$m^2\ g^{-1}$]	A_{Int} [b] [$m^2\ g^{-1}$]	A_{Ext} [c] [$m^2\ g^{-1}$]	V_{total} [d] [$cm^3\ g^{-1}$]	Pore sizes [e] [Å]
Lit. **fcu** UiO-66 [f]	700–1700	790–1600	98–101-	0.3–0.6	7, 11
10 eq.	1289	830	459	0.85	11, 29, 54, 89, 106
30 eq.	1253	896	357	0.65	14, 29, 50, 110
50 eq.	1072	825	247	0.39	7, 10, 27, 48, 103
Lit. **hcp** UiO-66 [g]	700–900	708–920	204	0.32–0.45	7, 10
100 eq.	912	708	204	0.35	7, 11, 26, 100, 154

[a] Multipoint BET between $p/p_0 = 0.01$ and 0.05. [b] Internal micropore surface area determined from *t*-plot and the *V*–*t* method. [c] External surface area, *i.e.*, the surface area from meso- and macropores, determined from the *t*-plot and *V*–*t* method. [d] Total pore volume at $p/p_0 \approx 0.8$. [e] Pore size distribution for UiO-66-10 eq. and -30 eq. determined from nitrogen sorption, for -50 eq. and -100 eq. by Ar sorption, see Section S6, ESI. [f] Depending on the used modulator.[3,52,58–62] [g] Values for A_{Int} and A_{Ext} are from our measurements.[49,53–55]

change much for the **fcu** UiOs when considering typical error margins or ±20 to 50 $m^2\ g^{-1}$. Yet, the smaller the amount of MAc modulator the higher the external surface area (A_{Ext}) or the lower the ratio of A_{Int} to A_{Ext}. The increased meso/macroporosity for smaller modulator amounts in the **fcu** UiOs is evident from the enhanced hysteresis when going from 50 eq. over 30 eq. to the 10 eq. sample (Fig. 3). The total pore volume V_{total} corresponds to the literature values of small sized **fcu** UiO-66 particles,[59] which range from 0.3 to 0.6 $cm^3\ g^{-1}$ [60] and to the **hcp** UiO-66, for which V_{total} values of 0.32 and 0.45 $cm^3\ g^{-1}$ were found.[53–55]

Pore size distribution (using the QSDFT method) and total pore volumes were calculated from nitrogen or argon (Ar) physisorption isotherms (Table 2 and Fig. S36 to S41, ESI†).

Pore size distribution by Ar sorption isotherms showed micropores of the same size as the triangular pore window (~6 Å), the tetrahedral pore (~8 Å) and the octahedral cage of **fcu** UiO-66 (at around 11 Å).[61] In defect-rich UiO-type structures the tetrahedral pore size is often increased from 8 Å to 10–12 Å, which is consistent with the presented data.[62] Also, for the **hcp** UiO the micropores of 7 and 10 Å are in good accordance with the literature values.[53] For all samples, additional mesopores above 2 nm (Table 2, Fig. S37, S39–S41, ESI†) can be due to linker defects or formed through agglomeration of small MOF particles by dithiol-bonds (see the SEM images in Fig. S4 and S5, ESI†).

Removal of silver(I)–ions from aqueous solutions

The above-determined UiO pore sizes should allow hydrated silver(I) ions to fit inside the pores of the thiol-functionalized MOFs for sorption from aqueous solutions. The literature states the diameter of a hydrated $AgNO_3$ ion pair in aqueous solution as 6.3 Å and for hydrated Ag^+ in solution as 4.8 Å. Both values refer to the distance from silver to the oxygen atoms of water in the first hydration shell.[63] Stability tests were carried out at pH 4, 7 and 10 with UiO-66-MAc-50 eq. and UiO-66-MAc-100 eq. to determine the potential pH range for the silver uptake experiments. Powder X-ray diffractograms show that UiO-66-MAc-50 eq. (Fig. S45, ESI†) is stable in water at pH 7 but loses crystallinity at pH 4 and decomposes at pH 10. The literature reported that UiO-66 is stable under acidic conditions up to pH 1 for extended periods,[5] while decomposing under basic conditions. For **hcp** UiO-66-MAc-100 eq. (Fig. S46, ESI†) the results show preservation of the structure at pH 7 and 4, whereas at basic conditions (pH 10) the material loses crystallinity. Ermer *et al.*[49] has shown stability for **hcp** UiO-66 from pH 0 to pH 12 over a period of three days. The lower pH-stability of the thiol-modified UiO-66 MOFs is reasoned by the high number of defects. Hence, the silver uptake experiments and the kinetic studies were carried out at pH 7, at which both MOFs tended to be stable for at least 24 h.

Removal of silver(I) from water was tested with UiO-66-MAc-50 eq., because of its high amount of incorporated sulfur-containing modulator. Additionally, **hcp** UiO-66-MAc-100 eq. was also tested for the removal of silver to check how the different structures influence the behavior for silver uptake. The maximum Ag(I) uptake for UiO-66-MAc-30 eq. was lower than that for UiO-66-MAc-50 eq. but slightly higher than that for UiO-66-MAc-100 eq., which we refer to as the lower and similar to slightly higher sulfur content of UiO-66-MAc-30 eq. compared to those of UiO-66-MAc-50 eq. and UiO-66-MAc-100 eq. (for the silver(I) uptake of UiO-66-MAc-30 eq. see Section S12, ESI†). Both UiO-66-MAc-materials exhibit a steep uptake of silver ions with increasing Ag-concentration, akin to a Type I isotherm. A plateau is reached at a concentration of 164 mg L^{-1} with an Ag^+ uptake of 84 mg g^{-1} for UiO-66-MAc-50 eq., and at a concentration of 216 mg L^{-1} with an Ag^+ uptake of 32 mg g^{-1} for UiO-66-MAc-100 eq. (Fig. 4). Both isotherms could be best fitted by a Langmuir adsorption isotherm model (Fig. 4b, details in Section S9, ESI†). Therefore, it corresponds well to previous reported uptake behaviors for the capture of Ag(I) and other heavy metal ions like Hg(II) with MOFs.[11,13,24]

The uptake depends on the incorporated sulfur amount, which is around 1.5 times higher in UiO-66-MAc-50 eq. over -100 eq. as determined in the CHNS analysis.

If the uptake of silver takes place at the thiol group of the MAc modulator then 38 mol% of the sulfur atoms in UiO-66-MAc-50 eq. become occupied by silver and 21 mol% in UiO-66-MAc-100 eq. SEM-EDX mappings after the uptake experiments for 12 h in 500 mg L^{-1} silver solution showed Ag to be evenly distributed over the MOF particles together with zirconium and sulfur (Fig. S53 and S54, ESI†). There are no significant silver EDX signals observed outside of the MOF particles, so it is verified that the decrease of silver concentration is solely due to the uptake in the MOF.

Porous materials like MOFs and COFs (covalent-organic frameworks) and also clay-type composite materials show a wide distribution in silver ion uptake capability between 8 and 450 mg g^{-1}. Most materials follow Langmuir-type adsorption

Open Access Article. Published on 16 December 2020. Downloaded on 2/10/2026 7:47:04 PM.
This article is licensed under a Creative Commons Attribution-NonCommercial 3.0 Unported Licence.

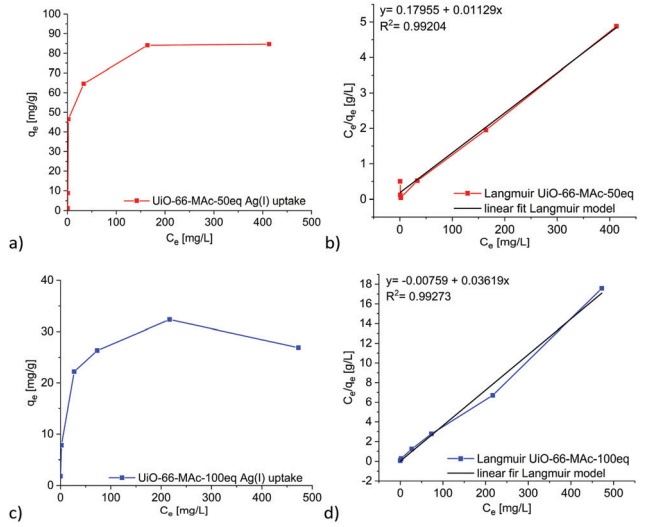

Fig. 4 Isotherms of the Ag(I) removal with UiO-66-MAc-50 eq. (a) and UiO-66-MAc-1000 eq. (c) (q_e = uptake at equilibrium; c_e= concentration at equilibrium). (b and d) Correlated fitted equilibrium data by the linearized Langmuir adsorption model.

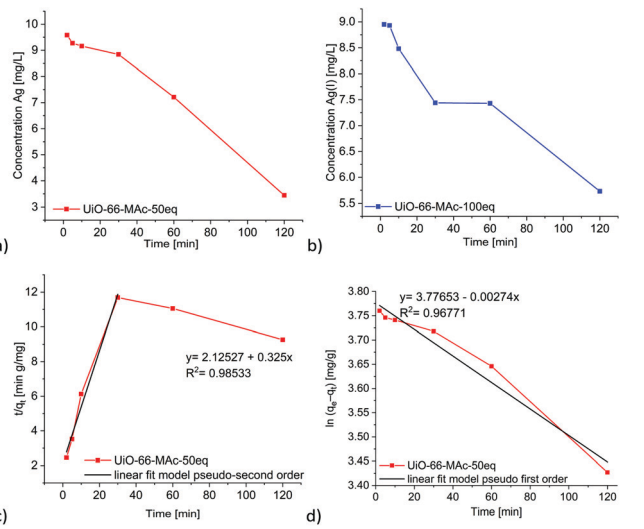

Fig. 5 Time-dependent removal of Ag(I) by UiO-66-MAc-50 eq. (a) and UiO-66-MAc-100 eq. (b) from a starting Ag^+ concentration of 10 mg L^{-1}. Linear fit for pseudo second-order kinetics (c) and for pseudo first-order kinetics (d) for the uptake in UiO-66-MAc-50 eq. See Fig. S48, ESI† for the linear fits for the uptake in UiO-66-MAc-100 eq.

models and the uptake can be described by chemisorption. For example, Ding *et al.* were able to reach a maximum uptake of 163 mg g^{-1} for their rhodanine (rd) post-functionalized UiO-66-NH_2-rd,[24] where each rhodanine moiety contains two accessible sulfur atoms. Conde-González *et al.* achieved a silver nanoparticle uptake of around 80 mg g^{-1} with HKUST-1.[42] Other materials show uptake between 8 mg g^{-1} for expanded perlite, which is a volcanic glass,[64] 35 mg g^{-1} for Fe_3O_4@SiO_2@TiO_2-IIP[65] (IIP = ion imprinted polymer), nearly 227 mg g^{-1} for a magnetite, thiourea and glutaraldehyde-modified chitosan resin[66] and up to 450 mg g^{-1} for a MgAl-layered double hydroxide[67] (a literature overview is provided in Table S11 in Section S15, ESI†).

Ding *et al.* observed a comparatively small Ag^+ uptake of 15 to 20 mg g^{-1} at a silver equilibrium concentration of 500 mg L^{-1} in pure UiO-66, which increases gradually with rising concentration.[24] While UiO-66-MAc-50 eq. reached the maximum uptake at a concentration of 200 mg L^{-1} Ag^+, pure UiO-66 reached the maximum of 20 mg g^{-1} at ~500 mg L^{-1}.[24] Therefore, the incorporation of thiol-groups into the framework enhances the sorbent–sorptive interactions, which is the affinity for silver, resulting in pore filling at very low concentrations. Ding *et al.* noticed the same effect for their rhodanine-modified UiO-66 derivates.[24] The introduced MAc modulator enhances the maximum specific uptake up to 4 times for UiO-66-MAc-50 eq. and around 1.5 times for **hcp** UiO-66-MAc-100 eq. compared to unfunctionalized UiO-66.

The kinetic silver uptake curves for UiO-66-MAc-50 eq. and -100 eq. (Fig. 5) were fitted to a pseudo second-order model until 30 minutes, when a change to pseudo first-order seemed to occur (Fig. 5 and Fig. S48, equations in Section S10, ESI†). Both models are often described for the removal of heavy metals from aqueous solutions with solid sorbents, including MOFs.[11,13,24,68]

We suggest that for the second-order kinetics both the silver and thiol concentrations determine the chemisorption of silver on easily accessible thiol groups, for example, at the outside of the particles and near the pore mouths. The chemisorption is then followed by the thiol groups inside the MOF pores, which is most likely diffusion controlled.[69,70]

X-ray photoelectron spectra show the oxidation state of silver in UiO-66-MAc-50 eq. and UiO-66-MAc-100 eq. as a mixture of predominantly Ag(0) and to a minor extent of Ag(I), indicating largely the reduction of silver(I) to silver(0) through the oxidation of thiol groups and for the remaining Ag(I) the formation of R–S–Ag bonds (for XPS spectra and detailed analysis see Section S13, ESI†). At the same time, the crystallinity of the UiO samples decreases in the presence of increasing silver concentration concomitant with the uptake (for PXRD and N_2-sorption see Section S13, ESI†). After the silver(I) uptake experiments nitrogen-sorption isotherms showed a significant loss in BET surface area (Fig. S51, ESI†) consistent with the intended pore filling. It was not possible to restore the BET surface area by regeneration through silver removal with KCN (Fig. S58, ESI†) This behavior was also reported by Ding *et al.* for their rhodanine-UiO-66-NH_2.[24] A possible regeneration of the Ag@UiO-66 samples was investigated through the silver extraction with potassium cyanide (KCN),[71] by formation of the dicyanoargentate(I) complex $[Ag(CN)_2]^-$. SEM-EDX verified the successful extraction of silver with KCN as only background noise was detected for silver at the MOF particles, yet the previous crystallinity of the MOF samples was not reinstated according to PXRD (see Section S13, ESI†).

Conclusion

We were able to reproducibly synthesize UiO-66 with the usage of Mac^- as a modulator, yielding a highly porous, microcrystalline UiO-66 with evenly distributed modulator as seen in the

© 2021 The Author(s). Published by the Royal Society of Chemistry

Open Access Article. Published on 16 December 2020. Downloaded on 2/10/2026 7:47:04 PM.
This article is licensed under a Creative Commons Attribution-NonCommercial 3.0 Unported Licence.

SEM-EDX mappings. The amount of incorporated modulator was thoroughly determined by several analytical techniques, whereas in the literature often only the defect characterization is used to quantify the amount of modulator.

UiO-66-MAc MOFs showed high sulfur contents for a modulated UiO-MOF with very high BET surface areas in the range of typical UiO-66 BET surface areas. The PXRD data for the products that were synthesized with 10, 30 and 50 eq. HMAc exhibited the typical **fcu** topology associated with UiO-66, whereas the synthesis with 100 eq. HMAc reproducingly yielded **hcp** UiO-66. To the best of our knowledge, this is the first functionalized **hcp** UiO-66.

The thiol-group was still intact after the synthesis as seen in the FT-Raman results. The presented synthesis route therefore offers a fast and cost-efficient possibility for the in-situ functionalization of UiO-66 with thiol groups. Mercaptoacetic acid as a modulator represents an affordable and easy way of introducing thiol groups into UiO-MOFs yielding high incorporated sulfur amounts of up to 7 wt%, while keeping the expected BET surface area of UiO-66.

The incorporation of Mac^- modulator ligands with free thiol groups led to enhanced uptake of Ag^+ from aqueous solutions when compared to non-functionalized UiO-66, with a maximum uptake of up to 84 mg g^{-1} for UiO-66-MAc-50 eq. and of 32 mg g^{-1} for UiO-66-MAc-100 eq. The uptake isotherms followed the Langmuir model and an initial pseudo second-order kinetics.

Conflicts of interest

There are no conflicts to declare.

Acknowledgements

We thank Dr T.-O. Knedel for his introduction to the atomic absorption spectrometer. We also thank Mrs Birgit Tommes for IR measurements.

Notes and references

1 C. Janiak and J. K. Vieth, *New J. Chem.*, 2010, **34**, 2366–2388.
2 H.-C. Zhou, J. R. Long and O. M. Yaghi, *Chem. Rev.*, 2012, **112**, 673–674.
3 G. C. Shearer, S. Chavan, S. Bordiga, S. Svelle, U. Olsbye and K. P. Lillerud, *Chem. Mater.*, 2016, **28**, 3749–3761.
4 J. B. DeCoste, G. W. Peterson, H. Jasuja, T. Grant Glover, Y. Huang and K. S. Walton, *J. Mater. Chem. A*, 2013, **1**, 5642–5650.
5 K. Leus, T. Bogaerts, J. De Decker, H. Depauw, K. Hendrickx, H. Vrielinck, V. Van Speybroeck and P. Van Der Voort, *Microporous Mesoporous Mater.*, 2016, **226**, 110–116.
6 (*a*) F. Vermoortele, B. Bueken, G. Le Bars, B. Van de Voorde, M. Vandichel, K. Houthoofd, A. Vimont, M. Daturi, M. Waroquier, V. Van Speybroeck, C. Kirschhock and D. E. De Vos, *J. Am. Chem. Soc.*, 2013, **135**, 11465–11468; (*b*) R. Limvorapitux, H. Chen, M. L. Mendonca, M. Liu, R. Q. Snurr and S. T. Nguyen, *Catal. Sci. Technol.*, 2019, **9**, 327–335.
7 (*a*) S. Chavan, J. G. Vitillo, D. Gianolio, O. Zavorotynsa, B. Civalleri, S. Jakobsen, M. H. Nilsen, L. Valenzano, C. Lamberti, K. P. Lillerud and S. Bordiga, *Phys. Chem. Chem. Phys.*, 2012, **14**, 1614–1626; (*b*) M. Waqas Anjum, F. Vermoortele, A. Laeeq Khan, B. Bueken, D. E. De Vos and I. F. J. Vankelecom, *ACS Appl. Mater. Interfaces*, 2015, **7**, 25193–25201.
8 (*a*) S. Rojas, I. Colinet, D. Cunha, T. Hidalgo, F. Salles, C. Serre, N. Guillou and P. Horcajada, *ACS Omega*, 2018, **3**, 2994–3003; (*b*) M. Nasrabadi, M. A. Ghasemzadeh and M. R. Z. Monfared, *New J. Chem.*, 2019, **43**, 16033–16040.
9 J. H. Cavka, S. Jakobsen, U. Olsbye, N. Guillou, C. Lamberti, S. Bordiga and K. P. Lillerud, *J. Am. Chem. Soc.*, 2008, **130**, 13850–13851.
10 G. C. Shearer, J. G. Vitillo, S. Bordiga, S. Svelle, U. Olsbye and K. P. Lillerud, *Chem. Mater.*, 2016, **28**, 7190–7193.
11 L. Huang, M. He, B. Chen and B. Hu, *J. Mater. Chem. A*, 2015, **3**, 11587–11595.
12 P. Yang, Y. Shu, Q. Zhuang, Y. Li and J. Gu, *Chem. Commun.*, 2019, **55**, 12972–12975.
13 P. Yang, Y. Shu, Y. Li and J. Gu, *Langmuir*, 2019, **35**, 16226–16233.
14 C. Wang, X. Liu, J. P. Chen and K. Li, *Sci. Rep.*, 2015, **5**, 16613.
15 Y. Fang, L. Zhang, Q. Zhao, X. Wang and X. Jia, *Chem. Pap.*, 2019, **73**, 1401–1411.
16 M. R. Azhar, H. R. Abid, V. Periasamy, H. Sun, M. O. Tade and S. Wang, *J. Colloid Interface Sci.*, 2017, **500**, 88–95.
17 S. Zaboon, H. R. Abid, Z. Yao, R. Gubner, S. Wang and A. Barifcani, *J. Colloid Interface Sci.*, 2018, **523**, 75–85.
18 C. Orellana-Tavra, R. J. Marshall, E. F. Baxter, I. Abánades Lázaro, A. Tao, A. K. Cheetham, R. S. Forgan and D. Fairen-Jimenez, *J. Mater. Chem. B*, 2016, **4**, 7697–7707.
19 H.-X. Zhao, Q. Zou, S.-K. Sun, C. Yu, X. Zhang, R.-J. Li and Y.-Y. Fu, *Chem. Sci.*, 2016, **7**, 5294–5301.
20 H. Molavi, M. Zamani, M. Aghajanzadeh, H. K. Manjili, H. Danafar and A. Shojaei, *Appl. Organomet. Chem.*, 2018, **32**, e4221.
21 K.-K. Yee, N. Reimer, J. Liu, S.-Y. Cheng, S.-M. Yiu, J. Weber, N. Stock and Z. Xu, *J. Am. Chem. Soc.*, 2013, **135**, 7795–7798.
22 L. Vial, R. F. Ludlow, J. Leclaire, R. Pérez-Fernández and S. Otto, *J. Am. Chem. Soc.*, 2006, **128**, 10253–10257.
23 M.-Q. Li, Y.-L. Wong, T.-S. Lum, K. S.-Y. Leung, P. K. S. Lam and Z. Xu, *J. Mater. Chem. A*, 2018, **6**, 14566–14570.
24 L. Ding, P. Shao, Y. Luo, X. Yin, S. Yu, L. Fang, L. Yang, J. Yang and X. Luo, *Chem. Eng. J.*, 2020, **382**, 123009.
25 J. C. McGreer, R. C. Playle, C. M. Wood and F. Galvez, *Environ. Sci. Technol.*, 2000, **34**, 4199–4207.
26 J. R. Morones, J. L. Elechiguerra, A. Camacho, K. Holt, J. B. Kouri, J. T. Ramírez and M. J. Yacaman, *Nanotechnology*, 2005, **16**, 2346–2353.
27 S. Kittler, C. Greulich, J. Diendorf, M. Köller and M. Epple, *Chem. Mater.*, 2010, **22**, 4548–4554.
28 A. Panáček, L. Kvítek, R. Prucek, M. Kolář, R. Večeřová, N. Pizúrovúá, V. K. Sharma, T. Nevěčná and R. Zbořil, *J. Phys. Chem. B*, 2006, **110**, 16248–16253.

Open Access Article. Published on 16 December 2020. Downloaded on 2/10/2026 7:47:04 PM.
This article is licensed under a Creative Commons Attribution-NonCommercial 3.0 Unported Licence.

29 T. M. Benn and P. Westerhoff, *Environ. Sci. Technol.*, 2008, **42**, 4133–4139.
30 J. Farkas, H. Peter, P. Christian, J. A. G. Urrea, M. Hassellöv, J. Tuoriniemi, S. Gustafsson, E. Olsson, K. Hylland and K. V. Thomas, *Environ. Int.*, 2011, **37**, 1057–1062.
31 S. Chernousova and M. Epple, *Angew. Chem., Int. Ed.*, 2013, **52**, 1636–1653.
32 D. Roe, B. Karandikar, N. Bonn-Savage, B. Gibbins and J.-B. Roullet, *J. Antimicrob. Chemoth.*, 2008, **61**, 869–876.
33 R. Kaegi, A. Voegelin, C. Ort, B. Sinnet, B. Thalmann, J. Krismer, H. Hagendorfer, M. Elumelu and E. Mueller, *Water Res.*, 2013, **47**, 3866–3877.
34 S. Takenaka, E. Karg, C. Roth, H. Schulz, A. Ziesenis, U. Heinzmann, P. Schramel and J. Heyder, *Environ. Health Perspect.*, 2001, **109**, 547–551.
35 P. V. AshaRani, G. Low Kah Mun, M. P. Hande and S. Valiyaveettil, *ACS Nano*, 2009, **3**, 279–290.
36 H. Bouwmeester, J. Poortman, R. J. Peters, E. Wijma, E. Kramer, S. Makama, K. Puspitaninganindita, H. J. P. Marvin, A. A. C. M. Peijnenburg and P. J. M. Hendriksen, *ACS Nano*, 2011, **5**, 4091–4103.
37 S. Wang, H. Li, X. Chen, M. Yang and Y. Qi, *J. Environ. Sci.*, 2012, **24**, 2166–2172.
38 B. Zhang, S. Wang, L. Fu, J. Zhao, L. Zhang and J. Peng, *Water, Air, Soil Pollut.*, 2018, **229**, 199.
39 C. Jeon, *Korean J. Chem. Eng.*, 2017, **34**, 384–391.
40 L. Ma, Q. Wang, S. M. Islam, Y. Liu, S. Ma and M. G. Kanatzidis, *J. Am. Chem. Soc.*, 2016, **138**, 2858–2866.
41 N. Pourreza, S. Rastegarzadeh and A. Larki, *J. Ind. Eng. Chem.*, 2014, **20**, 127–132.
42 J. E. Conde-González, E. M. Peña-Méndez, S. Rybáková, J. Pasán, C. Ruiz-Pérez and J. Havel, *Chemosphere*, 2016, **160**, 659–666.
43 R. G. Pearson, *J. Am. Chem. Soc.*, 1963, **85**, 3533–3539.
44 R. Thür, N. Van Velthoven, V. Lemmens, M. Bastin, S. Smolders, D. D. Vos and I. F. J. Vankelecom, *ACS Appl. Mater. Interfaces*, 2019, **11**, 44792–44801.
45 S. Øien, D. Wragg, H. Reinsch, S. Svelle, S. Bordiga, C. Lamberti and K. P. Lillerud, *Cryst. Growth Des.*, 2014, **14**, 5370–5372.
46 H. Wu, Y. S. Chua, V. Krungleviciute, M. Tyagi, P. Chen, T. Yildirim and W. Zhou, *J. Am. Chem. Soc.*, 2013, **135**, 10525–10532.
47 C. G. Piscopo, A. Polyzoidis, M. Schwarzer and S. Loebecke, *Microporous Mesoporous Mater.*, 2015, **208**, 30–35.
48 M. J. Cliffe, W. Wan, X. Zou, P. A. Chater, A. K. Kleppe, M. G. Tucker, H. Wilhelm, N. P. Funnell, F.-X. Coudert and A. L. Goodwin, *Nat. Commun.*, 2014, **5**, 4176.
49 M. Ermer, J. Mehler, M. Kriesten, Y. S. Avadhut, P. S. Schulz and M. Hartmann, *Dalton Trans.*, 2018, **47**, 14426–14430.
50 T. Zhao, L. Yang, P. Feng, I. Gruber, C. Janiak and Y.-J. Liu, *Inorg. Chim. Acta*, 2018, **471**, 440–445.
51 L. Yang, T. Zhao, I. Boldog, C. Janiak, X.-Y. Yang, Q. Li, Y.-J. Zhou, Y. Xia, D.-W. Lai and Y.-J. Liu, *Dalton Trans.*, 2019, **48**, 989–996.
52 L. Valenzano, B. Civalleri, S. Chavan, S. Bordiga, M. H. Nilsen, S. Jakobsen, K. P. Lillerud and C. Lamberti, *Chem. Mater.*, 2011, **23**, 1700–1718.
53 L. Zhou, S. Wang, Y. Chen and C. Serre, *Microporous Mesoporous Mater.*, 2019, **290**, 109674.
54 C. A. Clark, K. N. Heck, C. D. Powell and S. Wong, *ACS Sustainable Chem. Eng.*, 2019, **7**, 6619–6628.
55 X. Chen, Y. Lyu, Z. Wang, X. Qiao, B. C. Gates and D. Yang, *ACS Catal.*, 2020, **10**, 2906–2914.
56 M. Thommes, K. Kaneko, A. Neimark, J. Olivier, F. Rodriguez-Reinoso, J. Rouquerol and K. Sing, *Pure Appl. Chem.*, 2015, **87**, 1051–1069.
57 S. Tai, W. Zhang, J. Zhang, G. Luo, Y. Jia, M. Deng and Y. Ling, *Microporous Mesoporous Mater.*, 2016, **220**, 148–154.
58 C. Atzori, G. C. Shearer, L. Maschio, B. Civalleri, F. Bonino, C. Lamberti, S. Svelle, K. P. Lillerud and S. Bordiga, *J. Phys. Chem. C*, 2017, **121**, 9312–9324.
59 Y. Han, M. Liu, K. Li, Y. Zuo, Y. Wie, S. Xu, G. Zhang, C. Song, Z. Zhang and X. Guo, *CrystEngComm*, 2015, **17**, 6434–6440.
60 C. G. Piscopo, F. Trapani, A. Polyzoidis, M. Schwarzer, A. Pace and S. Loebbecke, *New J. Chem.*, 2016, **40**, 8220–8224.
61 M. Kim and S. M. Cohen, *CrystEngComm*, 2012, **14**, 4096–4104.
62 M. J. Katz, Z. J. Brown, Y. J. Colón, P. W. Siu, K. A. Scheidt, R. Q. Snurr, J. T. Hupp and O. K. Farha, *Chem. Commun.*, 2013, **49**, 9449–9451.
63 Y. Marcus, *Chem. Rev.*, 1988, **88**, 1475–1498.
64 H. Ghassabzadeh, A. Mohadespour, M. Torab-Mostaedi, P. Zaheri, M. G. Maragheh and H. Taheri, *J. Hazard. Mater.*, 2010, **177**, 950–955.
65 X. Yin, J. Long, Y. Xi and X. Luo, *ACS Sustainable Chem. Eng.*, 2017, **5**, 2090–2097.
66 A. M. Donia, A. A. Atia and K. Z. Elwakeel, *Hydrometallurgy*, 2007, **87**, 197–206.
67 L. Ma, Q. Wang, S. M. Islam, Y. Liu, S. Ma and M. G. Kanatzidis, *J. Am. Chem. Soc.*, 2016, **138**, 2858–2866.
68 F. Luo, K. L. Chen, L. L. Dang, W. N. Zhou, H. L. Lin, J. Q. Li, S. J. Liu and M. B. Luo, *J. Mater. Chem. A*, 2015, **3**, 9616–9620.
69 J. P. Simonin, *Chem. Eng. J.*, 2016, **300**, 254–263.
70 D. Robati, *J. Nanostruct. Chem.*, 2013, **3**, 55.
71 T. S. Ho, *Chem. Rev.*, 1975, **75**, 1–20.

© 2021 The Author(s). Published by the Royal Society of Chemistry